Journal of Materials Chemistry A

Accepted Manuscript

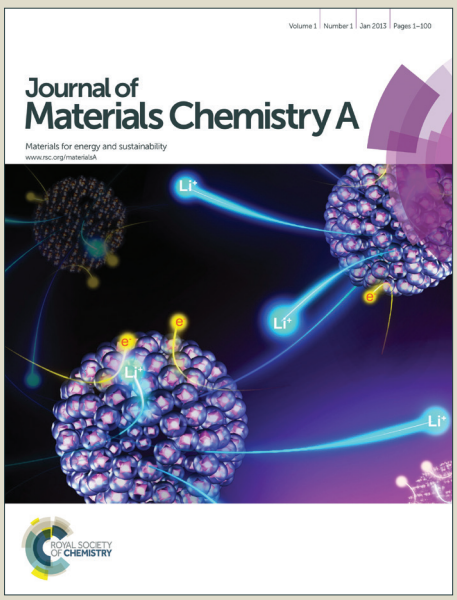

ROYAL SOCIETY OF CHEMISTRY

www.rsc.org/materialsA

Matching energy levels between TiO_2 and α-Fe_2O_3 in a core-shell nanoparticle for the visible-light photocatalysis

Zhaoyong Lin, Pu Liu, Jiahao Yan and Guowei Yang*

State Key Laboratory of Optoelectronic Materials and Technologies, Nanotechnology Research Center, School of Physics & Engineering, Sun Yat-sen University, Guangzhou 510275, Guangdong, P. R. China.

*Corresponding author: stsygw@mail.sysu.edu.cn

Abstract

Coupled TiO_2 with other semiconductors is a route to extend the optical response range of TiO_2 and improve the efficiency of photon quantum. α-Fe_2O_3 seems compatible with TiO_2 and possesses a high solar-light-harvesting capability that is fifteenth times as large as that of TiO_2. However, there is an energy level mismatch between TiO_2 and α-Fe_2O_3. The photocatalytic performance of TiO_2 would be inhibited when compositing with α-Fe_2O_3 due to the α-Fe_2O_3-induced photo-generated carriers trapping and dissipation. The composite acts like a one-way valve in which photo-generated carriers flow from a thick pipe to a thin one and then jam up. Herein, we have achieved the goal of matching energy levels between TiO_2 and α-Fe_2O_3 in core-shell nanoparticle for enhancing the visible-light photocatalysis. The heterostructured TiO_2@α-Fe_2O_3 core-shell nanoparticles were fabricated by long-pulsed laser ablation of a titanium target in water and a following hydrothermal

reaction. A well-matched interface between TiO_2 and α-Fe_2O_3 was observed, which promoting photo-generated electrons and holes migration and separation. The energy band of TiO_2 nanoparticle was demonstrated to be matched with that of α-Fe_2O_3, resulting from an upward shift of its valence band due to the abundant oxygen vacancies and bridging hydroxyls on its surface. In this situation, the "blocked pipe" seems to be dredged effectively and the visible-light photocatalytic methyl orange dyes degradation performance of the TiO_2@α-Fe_2O_3 nanoparticles was improved by a factor of two than that of the as-synthesized TiO_2 nanoparticles. These findings provided new insights into TiO_2 nanostructural photocatalyst and energy band engineering for the visible-light photocatalysis.

Introduction

Environmental pollution has come under the global spotlight in recent decades. For photocatalytic degradation of organic pollutants, TiO_2 nanomaterials have been used widely due to its high stability, super-hydrophilicity, non-toxicity and low cost.[1,2] However, its further application is limited by its low solar-light-harvesting capability and high photo-generated carriers recombination rate on account of its large bandgap and low electrical conductivity.[3,4] For improving its photocatalytic efficiency, it is desirable to develop heterostructured materials formed by jointing multiple semiconductor components together.[5] The foreign semiconductor is requested to be compatible with TiO_2 and possess high solar-light-harvesting capability. Hematite, α-Fe_2O_3, which is stable, abundant and nontoxic, may meet requirement.[6-8] α-Fe_2O_3 is believed to be n-type semiconductor with a small bandgap of 2.2 eV,[9] and its solar-light-harvesting capability has been demonstrated to be fifteenth times as large as that of TiO_2.[10] Moreover, α-Fe_2O_3/TiO_2 heterostructure may be easy to fabricate because of the high compatibility between α-Fe_2O_3 and TiO_2.[11-13]

Unfortunately, Serpone *et al.* reported that the photocatalytic performance of TiO_2 was inhibited when compositing with α-Fe_2O_3.[14] And Park *et al.* believed that it was due to the energy level mismatch between TiO_2 and α-Fe_2O_3.[10] In detail, the conduction band and valence band of α-Fe_2O_3 are located within the forbidden band of TiO_2, forming a typical straddling-type energy band structure.[5] In this situation, α-Fe_2O_3/TiO_2 heterostructure would act as a one-way valve under light irradiation,[14,15] in which photo-generated electrons and holes would both transfer to the surfaces of

α-Fe_2O_3 and recombine rapidly resulting from the poor conductivity, short hole diffusion length and high electron-hole recombination rate of α-Fe_2O_3.[9,16,17] In particular, a charge-mediating layer (SiO_2,[18] polyhydroxyl dextrin[6]) are needed when α-Fe_2O_3 and TiO_2 get together.

For these issues, herein, we report a simple route to synthesize the heterostructured TiO_2 @ α-Fe_2O_3 core-shell nanoparticles (NPs) to match the energy levels between TiO_2 and α-Fe_2O_3 by adjusting the energy band of TiO_2. Using a novel process involving laser ablation in liquid (LAL),[19] the as-synthesized TiO_2 NPs with abundant oxygen vacancies and bridging hydroxyls are demonstrated to show an upward shift of valence band to 2.50 eV, approaching that of α-Fe_2O_3. Meanwhile, the conduction band of TiO_2 is still above that of α-Fe_2O_3. Then, the as-synthesized TiO_2 NPs as the starting raw, the TiO_2 @ α-Fe_2O_3 core-shell NPs are fabricated by a treatment of hydrothermal reaction. Interestingly, these heterostructured NPs exhibit enhanced visible-light photocatalytic performance, and the energy level match is believed to be the most critical factor responsible for the enhanced performance. The well-matched interface between TiO_2 core and α-Fe_2O_3 shell in NPs is good for the photo-generated carrier migration and separation, as well. Furthermore, detailed photocatalytic mechanism based on the energy level mismatch and match is proposed. To the best of our knowledge, it is for the first time to directly match the energy levels between TiO_2 and α-Fe_2O_3 for the visible-light photocatalysis.

Experimental

TiO_2 NPs synthesis

TiO_2 NPs are synthesized by a LAL process. In this case, a titanium target with a purity of 99.99% is cleaned with ultrasonic oscillation in deionized water, ethanol, acetone, ethanol and deionized water, successively. Then, it is fixed on the bottom of a quartz chamber filled with 10 mL of deionized water. It is ablated by a Nd:YAG laser device for 50 min with a wavelength of 1064 nm, work current of 200 A, pulse width of 0.6 ms, repeating frequency of 5 Hz. The laser beam is focused to the surface of the metal target with a lens (200 mm). During the ablation process, the quartz chamber is dipped in a water tank to get rid of the overheating of the reaction water. After ablation, the blue colloid solution is transferred into a beaker and dried out at 50 ℃ to get blue solid powders.

TiO_2@α-Fe_2O_3 core-shell NPs fabrication

This fabrication is carried out by a hydrothermal reaction process. Typically, 20.0 mg of the as-synthesized TiO_2 powders are put into a clean beaker. For the fabrication of TiO_2@α-Fe_2O_3 core-shell NPs with different α-Fe_2O_3 loadings, 10 mL of 0.01 M, 0.02 M, 0.03 M $FeCl_3$ solutions are poured into the beaker, respectively. After ultrasonic oscillation for 20 min, the colloid solution is sealed in a 15-mL autoclave. The hydrothermal reaction lasts for 14 hours at 180 ℃. For comparison, α-Fe_2O_3 NPs are synthesized in the same way without TiO_2 powders. The concentration of $FeCl_3$ solution is selected to be 0.02 M. All the samples are taken out and cleaned repeatedly

with deionized water. After being dried out, the powders are collected for visible-light photocatalytic reactions directly.

Characterization

A thermal FE environment scanning electron microscope (SEM, Quanta 400, FEI Company) is used to observe the morphology of the products. Elemental composition analysis is carried out by an energy dispersive X-ray spectrometer (EDS, INCA, Oxford Company). Transmission electron microscopy (TEM), high-resolution TEM (HRTEM) and selected area electron diffraction (SEAD) are recorded by an FEI Tecnai G2 F30 transition electron microscope with a field-emission gun. The gravimetric titanium of the sample after laser ablation was measured using the inductively coupled plasma (ICP) method by an ICP-atomic Emission Spectrometry (ICP, IRIS(HR)). Typically, 2.0 mg of the sample and 10 g of ammonium sulfate was put into 20 mL of sulfuric acid (98%), and then kept in 100 ℃ by water bath heating with vigorous agitation for 10 h to make the sample react with sulfuric acid absolutely. The solution was then diluted with water and the concentration of the sample became 1.0 mg/L. Finally, 10 mL of the solution was extracted for ICP measurement. The structure of the sample is identified by an X-ray diffractometer (XRD, D/MAX-2200, Rigaku) under a voltage of 40 V and a current of 26 mA, and recorded with a speed of 1 $^{\circ}min^{-1}$. UV-Vis diffuse reflectance spectrum (DRS) is recorded in the range from 250 to 700 nm on a UV-Vis-NIR spectrophotometer (Lambda950, PerkinElmer Company) using $BaSO_4$ as a reference. Electron paramagnetic resonance (EPR) spectroscopy (EMX-10/12 plus, Bruker Company) is used to examine paramagnetic

species at 94K. High-resolution X-ray photoelectron spectroscopy (XPS) of Ti 2p and O 1s and valence band (VB) XPS are measured on XPS Scanning Microprobe spectrometer (Escalab 250, Thermo-VG Scientific, Al Kα) with respect to the position of the C 1s peak at 284.2 eV. The electrical conductivity of the TiO_2 sample was measured by the standard four-probe method at room temperature. The conductivity of non-doped TiO_2, prepared by anneal treatment of the self-doped TiO_2 at 800 ℃, was measured for comparison, as well. Before measurement, the powdered sample was ground for 30 min and pressed into disks with a diameter of 1 cm and a thickness of 3 mm. The surfaces of the disks were then coated with conducting silver paste for conductivity measurement. In addition, the structure of the annealed TiO_2 was identified by XRD.

Photocatalysis characterization

The photocatalytic performances of all the samples are measured toward degradation of methyl orange (MO) under the irradiation of a 300 W Xe lamp with a 420 nm cut-off filter at room temperature. Typically, the pre-synthesized sample is added to 25 mL of MO solution (10 mg L^{-1}) in a test-tube. The mixture is stirred in the dark for 30 min to establish an adsorption-desorption equilibrium between MO and the sample. The photodegradation experiment is conducted in a photochemical reactions instrument (Qiqian- III, Qiqian Company, China). The power density of light was measured to be 68.39 mW/cm^2 by an optical power meter. A pH meter was inset into the test-tube to monitor the pH value variation and H_2O_2 evolution in the whole process. 2.0 mL of the solution is drawn at given time intervals (2 min), and then

centrifuged at 6000 rpm for 20 min to remove the photocatalyst. The concentrations of MO solutions are determined by the absorbance at 464 nm using a UV-Vis-NIR spectrophotometer (Lamda900, PerkinElmer Company). To evaluate the mineralization process, total organic carbon (TOC) content measurement was conducted with a TOC-500 (Shimadzu). Moreover, the TiO_2@α-Fe_2O_3 NPs after the first cycle of photodegradation were collected by centrifugation and cleaned with deionized water for three times, and reused for subsequent five recycling tests to verify the stability.

Control experiments with radical scavengers are carried out in the same way. And the selected scavengers for photo-generated holes h^+, hydroxyl radicals ($\cdot OH$) and superoxide anion radicals ($\cdot O_2^-$) are ethylene diamine tetraacetic acid (EDTA, 0.7 mL, 0.1 M), tertiary butanol (tBuOH, 0.7 mL, 0.1 M) and nitrogen (N_2), respectively.

Results and Discussion

Characterization of TiO_2 NPs

Detailed morphology and structure characterizations of the as-synthesized TiO_2 NPs are performed by SEM, EDS, TEM, HRTEM and SAED, shown in Fig. 1. These results reveal that the synthesized blue colloid solution (inset in Fig. 1(a)) consists of spherical NPs with a typical size of 80 nm. The EDS spectrum exhibited in Fig. 1(b) shows that the as-synthesized NPs is composed of Ti and O elements, and the Si peak originates from the silicon wafer as a substrate for the SEM and corresponding EDS

characterization. According to the previous report, the colloid solution of TiO_2 NPs with abundant oxygen vacancies tends to show a color of blue, which is identical to our result.[20] According to the EDS analysis in the table in Fig. 1(b), the atomic ratio of Ti and O elements is determined to be about 1:1.47. Since the EDS analysis is always not accurate enough, ICP measurement is carried out. The Ti element content is 0.623 mg/L in the solution with a concentration of 1.0 mg/L, declaring that the O element content would be 0.377 mg/L. Therefore, the atomic ratio of Ti and O elements should be 1:1.77, still larger than 1:2 in non-doped TiO_2, indicating the as-synthesized NPs may be self-doped TiO_2 NPs, as well.

Further characterizations are needed. In detail, the HRTEM image, shown in Fig. 1(e), reveals that the interplanar spacing is 0.2856 nm, which corresponds to the (1,1,-1) crystallographic plane of TiO_2 with the monoclinic structure. In addition, the diffraction rings of SAED pattern in Fig. 1(f), signed by red arrows, correspond to the crystallographic planes of (1,1,-1), (2,0,0) and (0,2,2) of TiO_2 with the monoclinic structure, respectively. Note that the additional diffraction ring, signed by green arrows, does not correspond to any crystallographic plane of the monoclinic TiO_2. Micromesh study uncovers that it may correspond to the (1,-2,1) plane of Ti_9O_{17} with the triclinic structure. XRD pattern of the NPs is shown in Fig. 2(a), indicating that the coexistence of the TiO_2 with the monoclinic structure (PDF#48-1278) and Ti_9O_{17} with the triclinic structure (PDF#50-0791). The diffraction peaks at 2θ = 31.34°, 34.68° and 45.64° (marked by "#") belong to the (1,1,-1), (1,1,1) and (1,2,-1) planes of TiO_2, respectively. And the peaks at 2θ = 28.03° and 29.09°(marked by "*")

belong to the (1,-2,1) and (1,0,-1) planes of Ti_9O_{17}, respectively. The diffraction peaks of TiO_2 are more obvious and distinguishable than those of Ti_9O_{17}, and we can conclude that the main component of the products is TiO_2 NPs. Since the atomic ratio of Ti and O in TiO_2 is smaller than that of Ti_9O_{17}, Ti_9O_{17} is always regarded as a reduced TiO_2 species, and the coexistence of Ti_9O_{17} may be due to the abundant oxygen vacancies in TiO_2. However, there is no direct proof of whether the as-synthesized NPs are TiO_2 NPs with abundant oxygen vacancies or just mixtures of TiO_2 and Ti_9O_{17} NPs. Therefore, detailed characterization of energy band structure, surface chemical state and paramagnetic species in the NPs is carried out.

The TiO_2 NPs absorption plot (Fig. 2(b)) shows a band-edge at 450 nm and small absorption up to 650 nm in the visible light region, different from common TiO_2.[21] The calculating Tauc plot in Fig. 2(c) indicates an indirect bandgap of 2.58 eV for the as-synthesized TiO_2 NPs.[22] The valence band position of NPs is demonstrated to be 2.50 eV (*vs.* NHE) by linear extrapolation of the leading edges of VB XPS spectrum to the base line (Fig. 2(d)). Note that there are two linear regions in the VB XPS spectrum and the two extrapolation lines meet in the same point with the base line precisely. We believe that this offers a reminder that the as-prepared sample is an integrated whole instead of a mixture of TiO_2 and Ti_9O_{17}. Thereupon, the as-synthesized TiO_2 NPs with valence band at 2.50 eV and conduction band at -0.08 eV would exhibit a strong solar-light-harvesting capability. EPR is conducted to further confirm the presence of oxygen vacancies. As shown in Fig. 3(a), the as-synthesized TiO_2 NPs gives rise to a very strong and wide EPR signal at g = 1.953,

originating from the presence of paramagnetic Ti^{3+} centers.[23] In addition, the EPR signal seems to be very wide, indicating that there are different levels of oxygen vacancies in the sample.

The high resolution Ti 2p and O 1s XPS of the as-synthesized TiO_2 NPs are shown in Fig. 3(b-c). In Fig. 3(b), the two binding energy peaks are ascribed to the Ti $2p_{1/2}$ and Ti $2p_{3/2}$ core levels, respectively. In detail, the fitting of the two peaks reveals that both of them could be divided into two Gaussian peaks. The binding energy peaks at 464.7 and 458.7 eV can be attributed to the $2p_{1/2}$ and $2p_{3/2}$ core levels of Ti^{4+}, respectively. And those at 463.6 and 458.2 eV are related to the $2p_{1/2}$ and $2p_{3/2}$ core levels of Ti^{3+}, respectively.[20] According to the peaks area ratio, the ratio between Ti^{3+} and Ti^{4+} should be 0.63, revealing the existence of oxygen vacancies. Moreover, on the basis of the atomic ratio of Ti and O in the ICP results, the ratio between Ti^{3+} and Ti^{4+} could be determined to be 0.61, which is consistent with the XPS analysis within the margin of error. In Fig. 3(c), a well-defined peak at 529.9 eV can be observed, corresponding to the lattice oxygen in TiO_2. The shoulder at 531.7 eV can be attributed to bridging hydroxyls on the surfaces of TiO_2 NPs.[16,24] At this point, the existence of oxygen vacancies in the TiO_2 NPs are confirmed amply. According to Hong's report, the existence of bridging hydroxyls may originate from the reaction between water molecules and Ti clusters, jetting from the Ti target.[25] In addition, it is believed that O atoms in TiO_2 are easily removed and oxygen vacancies would form under the instantaneously high-temperature and high-pressure, created by LAL.[26] Note that there are abundant hydroxyls bridging on the surfaces of TiO_2 NPs and

affluent oxygen vacancies existing in them, which result in the upward shift of the valence band.[27]

It is believed that the introduction of oxygen vacancies into TiO_2 crystal would enhance its electrical conductivity greatly.[4] To further confirm the existence of oxygen vacancies, the electrical conductivity of the as-prepared TiO_2 NPs is conducted. For comparison, the conductivity of non-doped TiO_2 is measured, as well. As shown in Fig. 4(a), the annealed TiO_2 NPs do not show obvious changes except for a little irregularity. It is worth mentioning that this SEM image seems to be darker than that of the self-doped TiO_2 NPs in Fig. 1(a), indicating a poor conductivity of this annealed sample. Diffraction peaks of Ti_9O_{17} disappear in the XRD pattern in Fig. 4(b), demonstrating that the annealed NPs are pure monoclinic TiO_2 without doping. The conductivity results in Fig. 4(c) show that the self-doped TiO_2 NPs exhibit a conductivity of 6.1×10^{-3} S/cm while that of non-doped TiO_2 NPs is 1.7×10^{-7} S/cm, which is beneficial to photocatalytic performance.

Therefore, we can conclude that the self-doped TiO_2 NPs with abundant oxygen vacancies and bridging hydroxyls are synthesized by laser ablation of a Ti target in water. And these NPs exhibit a strong solar-light-harvesting capability with a suitable bandgap of 2.58 eV while the valence band and conduction band are located at 2.50 and -0.08 eV, respectively. It is worth mentioning that the self-doped TiO_2 NPs have been synthesized by a short-pulsed laser ablation in liquid (SP-LAL) for direct detection of H_2O_2 before.[20] However, the method used in our case is the so-called the long-pulsed laser ablation in liquid (LP-LAL), which is quite different from

SP-LAL.[28] It is believed that the product yield of SP-LAL is always 0.01 to 0.1 $\mu g\ min^{-1}$.[29] In this study, the blue colloid solution is collected and dried. Then, the powders are weighed and the product yield is calculated to be 0.4 $mg\ min^{-1}$, identical to the result of the previous report.[30] The product yield of LP-LAL is quite larger than that of SP-LAL, making it possible to apply the products in practice.

Characterization of TiO_2 @ α-Fe_2O_3 core-shell NPs

Typically, the TiO_2 @ α-Fe_2O_3 core-shell NPs are fabricated by a hydrothermal reaction between the as-synthesized TiO_2 NPs and $FeCl_3$ solution (0.02 M). As discussed above, the surface of the as-synthesized TiO_2 NPs is covered with abundant bridging hydroxyls, which can act as anchor sites for the implantation of Fe^{3+} and formation of α-Fe_2O_3 shell on it.[16] The morphology and structure characterization of typical TiO_2 @ α-Fe_2O_3 core-shell NPs are shown in Fig. 5. According to the XRD pattern in Fig. 5(a), the XRD pattern of TiO_2 NPs (marked by "#" and "*") do not show obvious change while five additional peaks at 2θ = 35.64°, 40.78°, 49.51°, 54.16° and 57.61° appear (marked by "^"). These five peaks correspond to the (1,1,0), (1,1,3), (2,0,2), (1,1,6) and (0,1,8) planes of α-Fe_2O_3 with a hexagonal structure (PDF#33-0664), respectively. The samples are spherical with a typical diameter of 95 nm (see Fig. 5(b)). The EDS pattern, shown in Fig. 5(c), demonstrates the coexistence of TiO_2 and α-Fe_2O_3, as well. In Fig. 5(d), the sample exhibits a core-shell structure with a 80-nm-large core and 7.5-nm-thick shell. Unfortunately, the HRTEM image of the joint of the core-shell structure in Fig. 5(e) is not clear enough. Therefore, a square area with an edge length of 2.5 nm is selected to conduct the fast

Fourier transformation (FFT) to obtain the electron diffraction patterns. After filtering out noise, inversing FFT (IFFT) is carried out.[31] From the IFFT image in Fig. 5(f), we can clearly see two areas with different interplanar spacing. The left one reveals the interplanar spacing is 0.2858 nm, which corresponds to the (1,1,-1) plane of TiO_2 with the monoclinic structure. The interplanar spacing in the right one is 0.2714 nm, corresponding to the (1,0,4) plane of α-Fe_2O_3. Therefore, the heterojunction is confirmed and the interface is well-matched (green dotted line in Fig. 5(f)).

In order to examine the influence of the thickness of α-Fe_2O_3 shell on the photocatalytic performance, the TiO_2 @ α-Fe_2O_3 core-shell NPs with different thicknesses of shells are synthesized through changing the concentration of $FeCl_3$ solution (0.01 M and 0.03 M). In addition, pure α-Fe_2O_3 NPs are synthesized for comparison. The results are shown in Fig. 6. The thicknesses of α-Fe_2O_3 shells are determined to be about 2 and 25 nm, respectively, shown in Fig. 6(a) and (b). The diameter of the as-synthesized α-Fe_2O_3 NPs is 300 nm. XRD patterns in Fig. 6(d) confirm the phase composition further, identical to our expectation. Note that the little leftward shift of the TiO_2 diffraction peaks may be because of the interaction between TiO_2 and α-Fe_2O_3.[32]

Photocatalytic reaction

The photocatalytic performances of TiO_2 @ α-Fe_2O_3 core-shell NPs with different thicknesses of shells are evaluated by the degradation of MO solution under visible light irradiation. For comparison, the photocatalytic MO degradation experiments of the as-synthesized TiO_2 and α-Fe_2O_3 NPs are carried out. In addition, the

self-photolysis of MO molecules without the addition of any photocatalysts is conducted, entitled "blank". As shown in Fig. 7(a), the absorbance of MO, whose characteristic absorption peak is set as 464 nm, decreases rapidly as the time prolongs. The relative concentration variation plots are recorded in Fig. 7(b). About 96.6% of MO is removed after 16 min photocatalysis. Since the concentration of initial MO solution is relatively low (C_{-30} =10 mg L^{-1}), we assume that the degradation process obeys the first-order kinetics. The plots of $-\ln(C/C_0)$ as a function of the irradiation time t are shown in Fig. 7(c), where C_0 means the MO concentration after the adsorption-desorption equilibrium. The slope of the fitting line can be regarded as the corresponding degradation rate. Note that the as-synthesized TiO_2 NPs can also show a good visible-light photocatalytic performance due to their enhanced solar-light-harvesting capability, resulting from the narrowing of their bandgap.

As above, the existence of oxygen vacancies and bridging hydroxyls may result in the insertion of intermediate energy levels in the forbidden band gap and then the narrowing of their bandgap.[2] Moreover, the introduction of affluent oxygen vacancies in our case can enhance the electrical conductivity very much, which is beneficial to the photocatalytic performance.[23] The degradation rates for all the samples are described in the histogram in Fig. 7(d), indicating that the degradation rate experiences a process of raising and following declining as the thickness of α-Fe_2O_3 shell increases. The typical TiO_2 @ α-Fe_2O_3 NPs with a shell of 7.5 nm, fabricated with 0.02 M $FeCl_3$ solution, seem to behave best.

To evaluate the mineralization process, TOC content variations during the degradation are recorded in Fig. 8. We can clearly see that the TOC contents decline rapidly. The TOC contents before and after photocatalysis are measured to be 5.684 and 0.208 mg/L, showing that the TOC removal is 96.3%. This result is consistent with the MO removal. We can conclude that the MO is degraded instead of being removed in our case.

Recycling photocatalytic degradation experiments are carried out for six times to verify the stability of the TiO_2 @ α-Fe_2O_3 NPs. As shown in Fig. 9(a), the photocatalytic performance after six cycles does not behave significant decrease. The negligible decline of their activity may be due to powder lost during centrifugation and wash. The XRD pattern of the six times recycled sample in Fig. 9(b) is nearly identical to the original pattern in Fig. 5(a), guaranteeing the photo-stability of the TiO_2 @ α-Fe_2O_3 NPs.

In the previous reports, Fenton reaction is required in the photocatalytic dyes degradation experiments of α-Fe_2O_3.[1,2,12,16,33] In Fenton reaction, Fe^{3+} ions are reduced to Fe^{2+} ions by the photo-generated electrons first, and then Fe^{2+} ions are oxidized to Fe^{3+} ions again by the external H_2O_2 solution, as described in Eqs. (1) and (2).

$$Fe^{3+} + e^- \rightarrow Fe^{2+} \quad (1)$$

$$Fe^{2+} + H_2O_2 \rightarrow Fe^{3+} + \cdot OH + OH^- \quad (2)$$

In another way, hydroxyl radicals $\cdot OH$ can be produced by the reactions listed as follow.[34]

$$h^+ + H_2O \rightarrow H^+ + \cdot OH \quad (3)$$

$$h^+ + OH^- \rightarrow \cdot OH \quad (4)$$

$$e^- + O_2 \rightarrow \cdot O_2^- \quad (5)$$

$$e^- + 2H^+ + \cdot O_2^- \rightarrow H_2O_2 \quad (6)$$

$$e^- + H_2O_2 \rightarrow \cdot OH + OH^- \quad (7)$$

Although external addition of H_2O_2 is not needed, it can also be brought in because of the reaction (6). It is believed that $\cdot OH$ is the main active species in Fenton reaction. Therefore, the controlling experiment with tBuOH as the scavenger of $\cdot OH$ is carried out to elucidate whether Fenton reaction takes place or not. As shown in Fig. 10, the photocatalytic performance of typical TiO_2 @ α-Fe_2O_3 NPs is hardly affected with the addition of tBuOH. This result indicates that $\cdot OH$ does not play a key role in the photocatalytic performance, and Fenton reaction is not involved in our case. In addition, the reactions (3), (4) and (7) are insignificant, as well. At this point, it is of great importance to explore the main active species in this process to figure out the mechanism. In Fig. 10 (d), the pH of the solution during the photodegradation is monitored, and it keeps 6.9, showing no variation. Since the reaction (6) is less likely to happen in near-neutral environment and it should happen on the basis of the reaction (5), we make an assumption that the reaction (5) is the most pivotal, and $\cdot O_2^-$ should be the main active species. Therefore, an anaerobic environment is constructed by continuous blowing of N_2 into the reaction system to inhibit the generation of $\cdot O_2^-$. We can see that the photocatalytic performance is greatly suppressed, even poorer than pure α-Fe_2O_3, giving evidence of our assumption.

Moreover, photo-generated holes are consumed with the addition of EDTA to investigate their function in this photocatalytic reaction. Excitingly, the photocatalytic performance is demonstrated to be improved a little by consuming the holes. The holes seem to play a negative role. We believe that it is because of the suppression of the recombination between electrons and holes by consuming the holes. Once the recombination is inhibited, more electrons could be offered for the happen of the reaction (5) and more $\cdot O_2^-$ species works. This can further verify our assumption that $\cdot O_2^-$ is the main active species.

Based on the above discussion and analysis, a possible photocatalytic mechanism is proposed, as illustrated in Fig. 11. For the common white TiO_2, when compositing with α-Fe_2O_3, a straddling energy band structure would form, resulting in the energy level mismatch between them. When irradiated under the visible light, TiO_2 is not activated and the composite just acts as α-Fe_2O_3 with high carrier recombination rate. When irradiated under the ultraviolet light, photo-generated electrons and holes in TiO_2 would migrate to α-Fe_2O_3 simultaneously, and recombine rapidly due to the accumulation of electrons and holes in α-Fe_2O_3 and its poorer conductivity. In this situation, the composite acts like a one-way valve in which carriers flow from a thick pipe to a thin one and then jam up. By this time, "pipe dredging" by matching the energy levels between TiO_2 and α-Fe_2O_3 brooks no delay.

In our case, the valence band of the self-doped TiO_2 NPs is demonstrated to be located in 2.50 eV (*vs.* NHE), which is in close proximity to that of α-Fe_2O_3 (2.48 eV). And the conduction band of blue TiO_2 is still above that of α-Fe_2O_3. When the

TiO_2 @ α-Fe_2O_3 core-shell NPs are under the irradiation of visible light, both of TiO_2 and α-Fe_2O_3 are activated and electrons and holes stay tentatively on their own conduction and valence bands. Thanks to the excellent conductivity of blue TiO_2 and the well-matched interface, these carriers can migrate across the interface at a high speed, which is critical for the photocatalytic performance. It is believed that the built-in electrical field between two semiconductors would promote the carriers migration across the interface and inhibit the electron-hole recombination.[35,36,37] And a hole-flowing equilibrium would establish quickly since the two valence bands are adjacent. Electrons on the TiO_2 conduction band would jump to that of α-Fe_2O_3 under the driving force of the energy level difference. As is known, α-Fe_2O_3 possesses an excellent adsorption capacity of oxygen molecules.[38] Therefore, electrons on the surface of α-Fe_2O_3 would be captured and trapped by the adsorbed O_2 molecules, and then main active species $\cdot O_2^-$ is generated, which is beneficial to the separation of electron-hole pairs.[39] As a result, MO molecules are degraded quickly. Certainly, electrons would be consumed by holes partly and the photocatalytic performance should be improved by depleting holes with the addition of EDTA. There is no doubt that the visible light photocatalytic performance of the as-synthesized TiO_2 has been increased by a factor of two through the forming of the well-matched TiO_2/α-Fe_2O_3 heterostructure. However, the performance is inhibited with the successive increase of the α-Fe_2O_3 shell thickness, which is on account of the finite light penetration depth of α-Fe_2O_3 and the weakening of the photoresponse of TiO_2 core.[17] It is no doubt that the photo-generated electrons can easily transfer to O_2

on the surfaces to form active specials. But the holes cannot be quickly consumed, which will prevent the continuous charge separation more or less. Therefore, other well-designed hybrid nanostructures may be helpful, such as inlaid, interspersed, Janus and yolk-shell structures.[40,41,42] And further effort is needed in our subsequent work.

Conclusions

In summary, the heterostructured TiO_2 @ α-Fe_2O_3 core-shell NPs have been fabricated by a well-designed route of LP-LAL for TiO_2 core and following hydrothermal reaction for α-Fe_2O_3 shell. The as-fabricated TiO_2 @ α-Fe_2O_3 NPs with a typical shell thickness of 7.5 nm were demonstrated to exhibit excellent visible-light photocatalytic dyes degradation performance, breaking the traditional concept that TiO_2/α-Fe_2O_3 composite usually shows poor photocatalytic performance due to the energy level mismatch between TiO_2 and α-Fe_2O_3. In our case, we have successfully achieved the goal of matching the energy levels by rising the valence band of the TiO_2 core to that of α-Fe_2O_3 with the help of the abundant oxygen vacancies and bridging hydroxyls on its surface. The energy level match is believed to be the most critical factor for the photocatalytic activity. The narrowing of bandgap, resulting from the rise of valence band, endows the TiO_2 core with splendid solar-light-harvesting capability. An improved electrical conductivity is acquired thanks to the oxygen vacancies. And the photo-generated electron-hole pair separation ability is promoted on account of the well-matched interface and the adsorbed O_2. $\cdot O_2^-$ is identified to be

the most active species, instead of ·OH, disavowing the participation of Fenton reaction. By adjusting the energy band, the energy level match between different semiconductors could be achieved for the enhanced visible-light photocatalysis. These findings actually open a door to broad applicability of the LAL technique for energy band engineering.

Acknowledgements. The National Basic Research Program of China (2014CB931700) and the State Key Laboratory of Optoelectronic Materials and Technologies of Sun Yat-sen University supported this work.

References

1 E. S. Mora, E. G. Barojas, E. R. Rojas and R. S. González, *Solar Energy Materials & Solar Cells*, 2007, **91**, 1412-1415.

2 K. Nishijima, Y. Fujisawa, N. Murakami, T. Tsubota and T. Ohno, *Applied Catalysis B: Environmental*, 2008, **84**, 584-590.

3 G. M. Wang, H. Y. Wang, Y. C. Ling, Y. C. Tang, X. Y. Yang, R. C. Fitzmorris, C. C. Wang, J. Z. Zhang and Y. Li, *Nano Lett.*, 2011, **11**, 3026-3033.

4 J. Su, X. X. Zou and J.-S. Chen, *RSC Adv.*, 2014, **4**, 13979-13988.

5 Y.-P. Yuan, L.-W. Ruan, J. Barber, S. C. J. Loo and C. Xue, *Energy Environ. Sci.*, 2014, **12**, 3937-3951.

6 A. I. Kontos, V. Likodimos, T. Stergiopoulos, D.S. Tsoukleris and P. Ealaras, *Chem. Mater.*, 2009, **21**, 662-672.

7 S. K. Mohapatra, S. Banerjee and M. Misra, *Nanotechnology*, 2008, **19**, 315601-315607.

8 M. Zhang, Y. J. Lin, T. J. Mullen, W.-F. Lin, L.-D. Sun, C.-H. Yan, T. E. Patten, D. W. Wang and G.-Y. Liu, *J. Phys. Chem. Lett.*, 2012, **3**, 3188-3192.

9 C. J. Sartoretti, B. D. Alexander, R. Solarsks, I. A. Rutkowska and J. Augustynski, *J. Phys. Chem. B*, 2005, **109**, 13685-13692.

10 T. H. Jeon, W. Choi and H. Park, *J. Phys. Chem. C*, 2011, **115**, 7134-7142.

11 J. A. Navio, G. Colon, M. Macias, C. Real and M. I. Litter, *Applied Catalysis A: Gerneral*, 1999, **177**, 111-120.

12 L. Qin, X. X. Pan, L. Wang, X. P. Sun, G. L. Zhang and X. W. Guo, *Applied Catalysis B: Environmental*, 2014, **150-151**, 44-553.

13 M. Z. Lin, H. Chen, W. F. Chen, A. Nakaruk, P. Koshy and C. C. Sorrell, *International Journal of Hydrogen Energy*, 2014, **39**, 21500-21511.

14 N. Serpone, P. Maruthamuthu, P. Pichat, E. Pelizzetti and H. Hidaka, *Journal of Photochemistry and Photobiology A: Chemsitry*, 1995, **85**, 247-255.

15 Y. Bessekhouad, D. Robert and J.-V. Weber, *Catalysis Today*, 2005, **101**, 315-321.

16 S. C. Han, L. F. Hu, Z. Q. Liang, S. Wageh, A. A. Al-Ghamdi, Y. S. Chen and X. S. Fang, *Adv. Funct. Mater.*, 2014, **24**, 5719-5727.

17 T. K. Townsend, E. M. Sabio, N. D. Browning and F. E. Osterloh, *Energy Environ. Sci.*, 2011, **4**, 4270-4275.

18 X. Y. Li, D. P. Liu, S. Y. Song and H. J . Zhang, *Cryst. Growth Des.*, 2014, **14**, 5506-5511.

19 G. W. Yang, *Progress in Materials Science*, 2007, **52**, 648-698.

20 S. S. Pan, W. Lu, Y. H. Zhao, W. Tong, M. Li, L. M. Jin, J. Y. Choi, F. Qi, S. G. Chen, L. F. Fei and S. F. Yu, *ACS Appl. Mater. Interfaces*, 2013, **5**, 12784-12788.

21 J. Schneider, M. Matsuoka, M. Takeuchi, J. L. Zhang, Y. Horiuchi, M. Anpo and D. W. Bahnemann, *Chem. Rev.*, 2014, **114**, 9919-9986.

22 J. Xiao, Q. L. Wu, P. Liu, Y. Liang, H. B. Li, M. M. Wu and G. W. Yang, *Nanotechnology*, 2014, **25**, 135702-135711.

23 H. Li, J. Q. Chen, Z. B. Xia and J. H. Xing, *J. Mater. Chem. A*, 2015, **3**, 699-705.

24 X. B. Chen, L. Liu, P. Y. Yu and S. S. Mao, *Science*, 2011, **331**, 746-750.

25 S. M. Hong, S. Lee, H. J. Jung, Y. Yu, J. H. Shin, K.-Y. Kwon and M. Y. Choi, *Bull. Korean Chem. Soc.*, 2013, **34**, 279-282.

26 Y. Takeda and F. Mafune, *Chemical Physics Letters*, 2014, **599**, 110-115.

27 L. D. Li, J. Q. Yan, T. Wang, Z.-J. Zhao, J. Zhang, J. L. Gong and N. J. Guan, *Nature Communications*, 2015, **6**, DOI: 10. 1038/ncomms6881.

28 K. Y. Niu, J. Yang, S. A. Kulinich, J. Sun, H. Li and X. W. Du, *J. Am. Chem. Soc.*, 2012, **132**, 9814-9819.

29 N. Barsch, J. Jakobi, S. Weiler and S. Barcikowski, *Nanotechnology*, 2009, **20**, 445603-445611.

30 K. Y. Niu, J. Yang, S. A. Kulinich, J. Sun and X. W. Du, *Langmuir*, 2010, **26**, 16652-16657.

31 D. J. Yang, H. W. Liu, Z. F. Zheng, Y. Yuan, J.-C. Zhao, E. R. Waclawik, X. B. Ke and H. Y. Zhu, *J. Am. Chem. Soc.*, 2009, **131**, 17885-17893.

32 Z. H. Xu and J. G. Yu, *Nanoscale*, 2011, **3**, 3138-3144.

33 T. Ohno, Z. Miyamoto, K. Nishijima, H. Kanemitsu and F. Xueyuan, *Applied Catalysis A: General*, 2006, **302**, 62-68.

34 Z. Y. Lin, J. Xiao, J. H. Yan, P. Liu, L. H. Li and G. W. Yang, *J. Mater. Chem. A*, 2015, **3**, 7649-7658.

35 S. S. Huang, Q. Q. He, J. T. Zai, M. Wang, X. M. Li, B. Li and X. F. Qian, *Chem. Commun.*, 2015, **51**, 8950-8953.

36 M. Xu, T. N. Ye, F. Dai, J. D. Yang, J. M. Shen, Q. Q. He, W. L. Chen, N. Liang, J. T. Zai and X. F. Qian, *ChemSusChem*, 2015, **8**, 1218-1225.

37 Q. Q. He, S. S. Huang, C. Wang, Q. Q. Qiao, N. Liang, M. Xu, W. L. Chen, J. T. Zai and X. F. Qian, *ChemSusChem*, 2015, **8**, 817-820.

38 Q. Y. Hao, L. M. Li, X. M. Yin, S. Liu, Q. H. Li and T. H. Wang, *Materials Science and Engineering B*, 2011, **176**, 600-605.

39 L. M. He, L. Q. Jing, Z. J. Li, W. T. Sun and C. Liu, *RSC Adv.*, 2013, **3**, 7438-7444.

40 R. B. Jiang, B. X. Li, C. H. Fang and J. F. Wang, *Adv. Mater.*, 2014, **26**, 5274-5309.

41 N. Liang, J. T. Zai, M. Xu, Q. Zhu, X. Wei and X. F. Qian, *J. Mater. Chem. A*, 2014, **2**, 4208-4216.

42 N. Liang, M. Wang, L. Jin, S. S. Huang, W. L. Chen, M. Xu, Q. Q. He, J. T. Zai, N. H. Fang and X. F. Qian, *ACS Appl. Mater. Interfaces*, 2014, **6**, 11698-11705.

Figure Captions

Fig. 1 Morphology and structure of the as-synthesized TiO_2 NPs. (a) SEM image (inset: photograph of the as-synthesized blue colloid solution), (b) EDS spectrum, (c) TEM image at low magnification, (d) TEM image at high magnification, (e) HRTEM image, and (f) SEAD pattern of the products.

Fig. 2 (a) XRD pattern, (b) UV-Vis absorption spectrum, (c) Tauc plot, and (d) VB XPS spectrum of the as-synthesized TiO_2 NPs**.**

Fig. 3 Characterization about self-doping: (a) EPR spectrum at 94 K, (b) Ti 2p XPS spectrum, and (c) O 1s XPS spectrum of the as-synthesized TiO_2 NPs**.**

Fig. 4 (a) SEM image and (b)XRD pattern of the annealed TiO_2 NPs. (c) Comparison of the electrical conductivities of the as-prepared and annealed TiO_2 NPs.

Fig. 5 Morphology and structure of the as-fabricated TiO_2@α-Fe_2O_3 core-shell NPs. (a) XRD pattern, (b) SEM image, (c) EDS spectrum, (d) TEM image, (e) HRTEM image, and (f) IFFT image of the selected area of the typical TiO_2@α-Fe_2O_3 NPs fabricated with 0.02 M $FeCl_3$ solution.

Fig. 6 (a) SEM and TEM (inset) images of the TiO_2@α-Fe_2O_3 NPs fabricated with 0.01 M $FeCl_3$ solution. (b) SEM and TEM (inset) images of the TiO_2@α-Fe_2O_3 NPs fabricated with 0.03 M $FeCl_3$ solution. (c) SEM and TEM (inset) images of α-Fe_2O_3 NPs. (d) The corresponding XRD patterns.

Fig. 7 (a) UV-Vis spectral changes of MO solution. (b) The relative concentration variation plots of MO solution. (c) $-\ln(C/C_0)$ *vs*. t plots. (d) The corresponding photocatalytic rates statistical histograms.

Fig. 8 TOC changes of the MO solution.

Fig. 9 (a) Recycling experiments of the photocatalytic degradation of MO. (b) XRD pattern of the TiO_2@α-Fe_2O_3 NPs after six recycling experiments.

Fig. 10 Control experiments with radical scavengers. (a) The relative concentration variation plots of MO solution. (b) $-\ln(C/C_0)$ *vs*. t plots. (c) The corresponding photocatalytic rates statistical histograms. (d) The pH value variation statistical histograms.

Fig. 11 Schematic illustration of the visible-light photocatalytic mechanisms based on energy levels mismatch (left) and match (right) between TiO_2 and α-Fe_2O_3.

Fig. 1

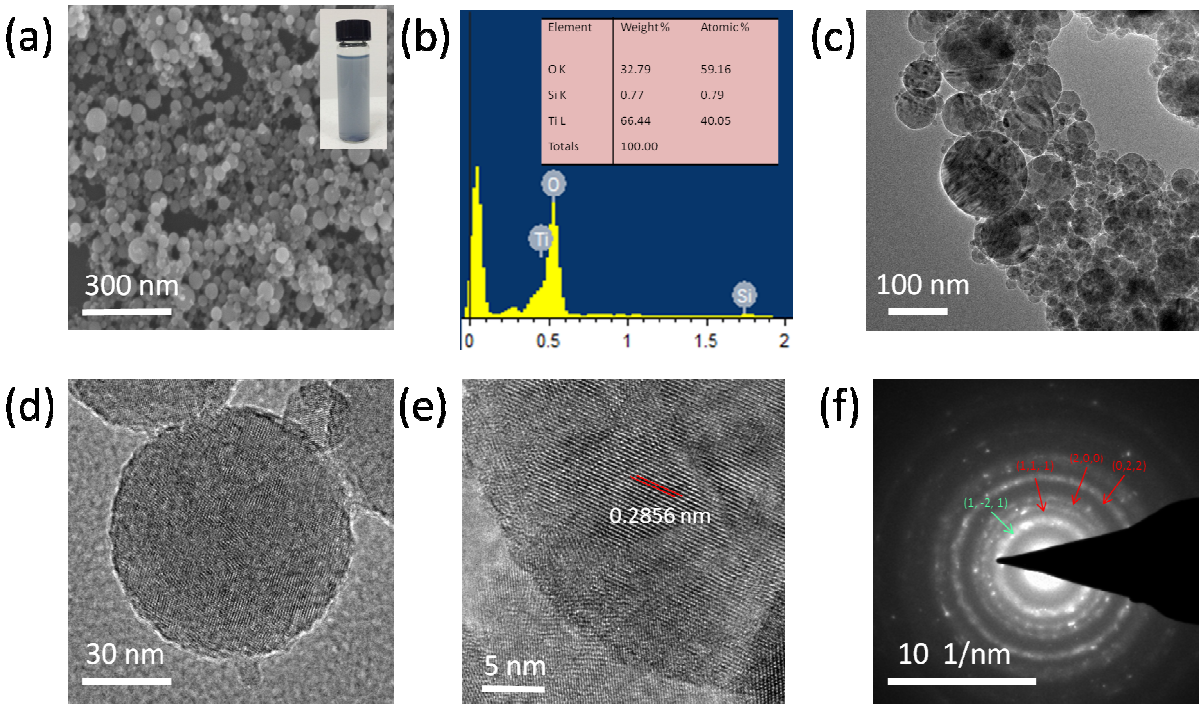

Fig. 2

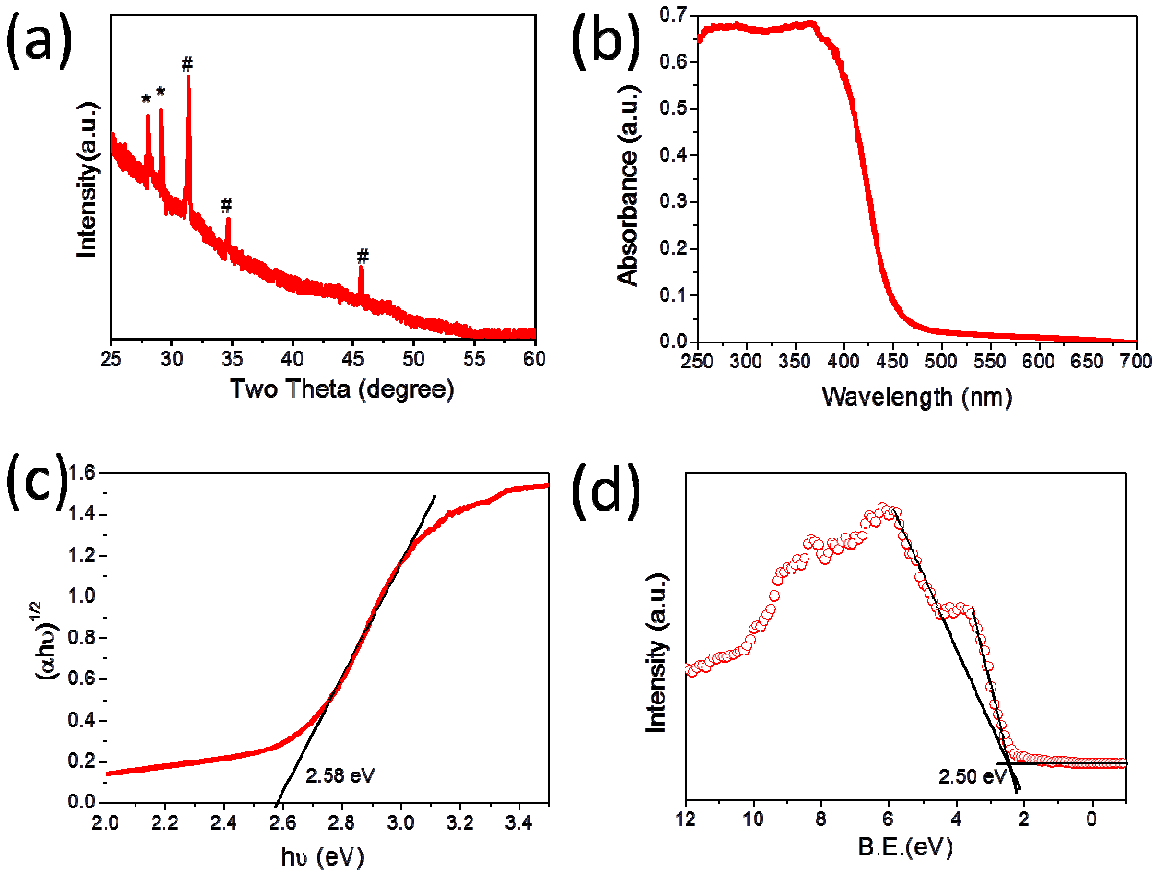

Fig. 3

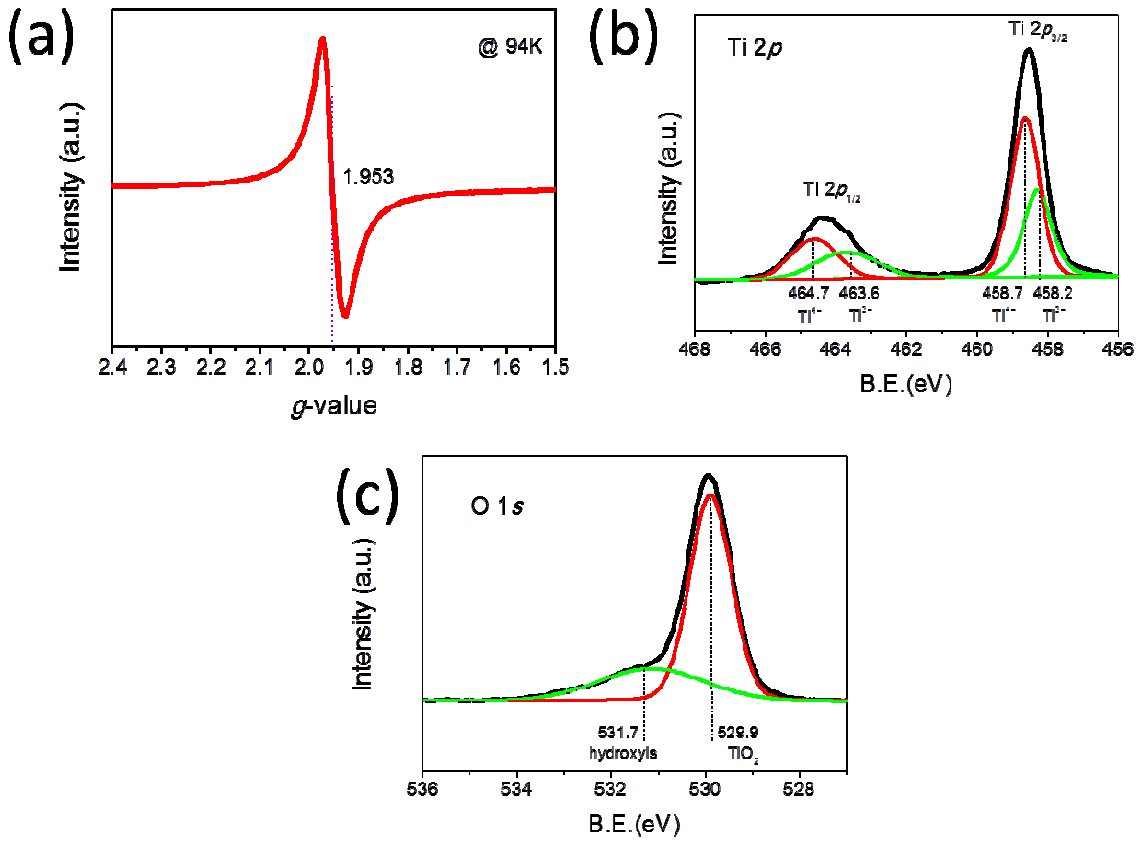

Fig. 4

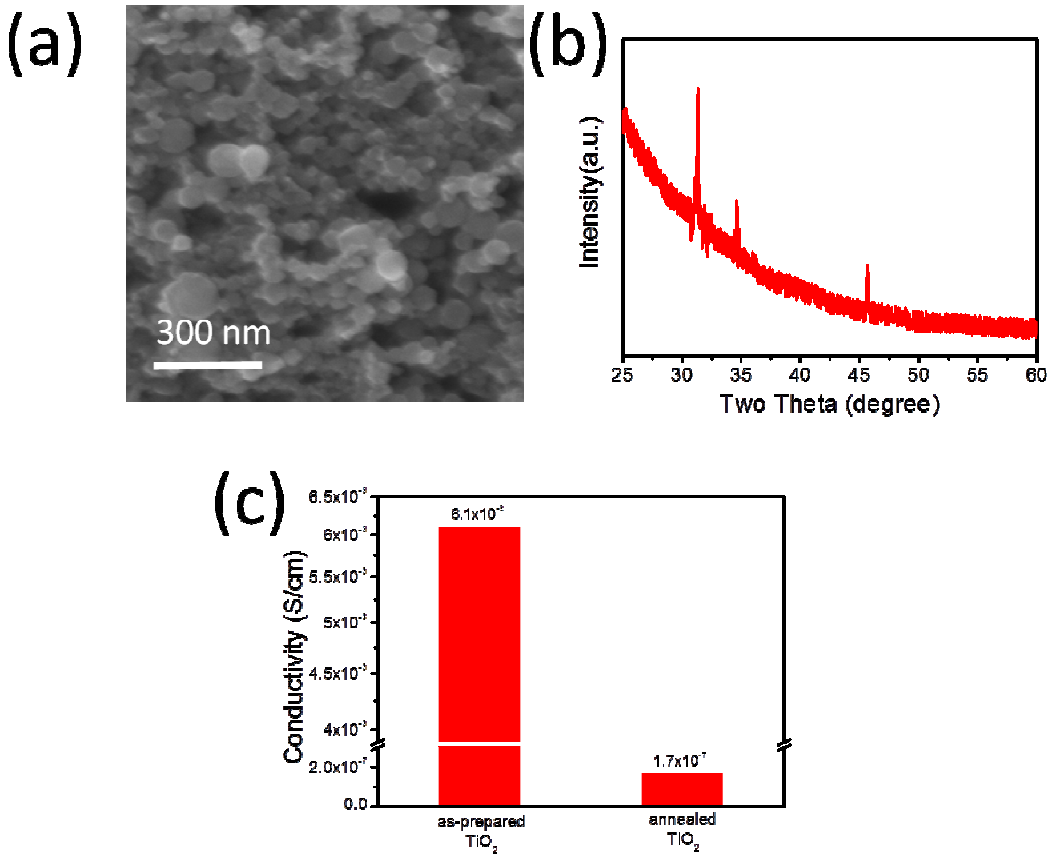

Fig. 5

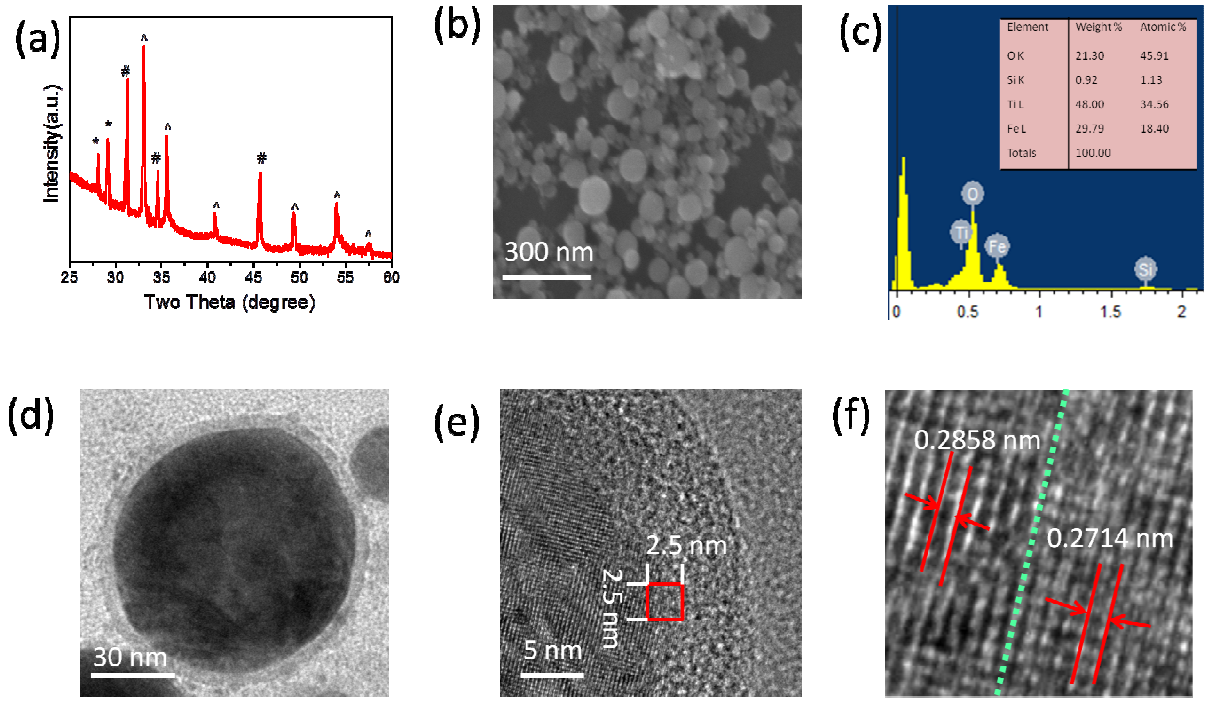

Fig. 6

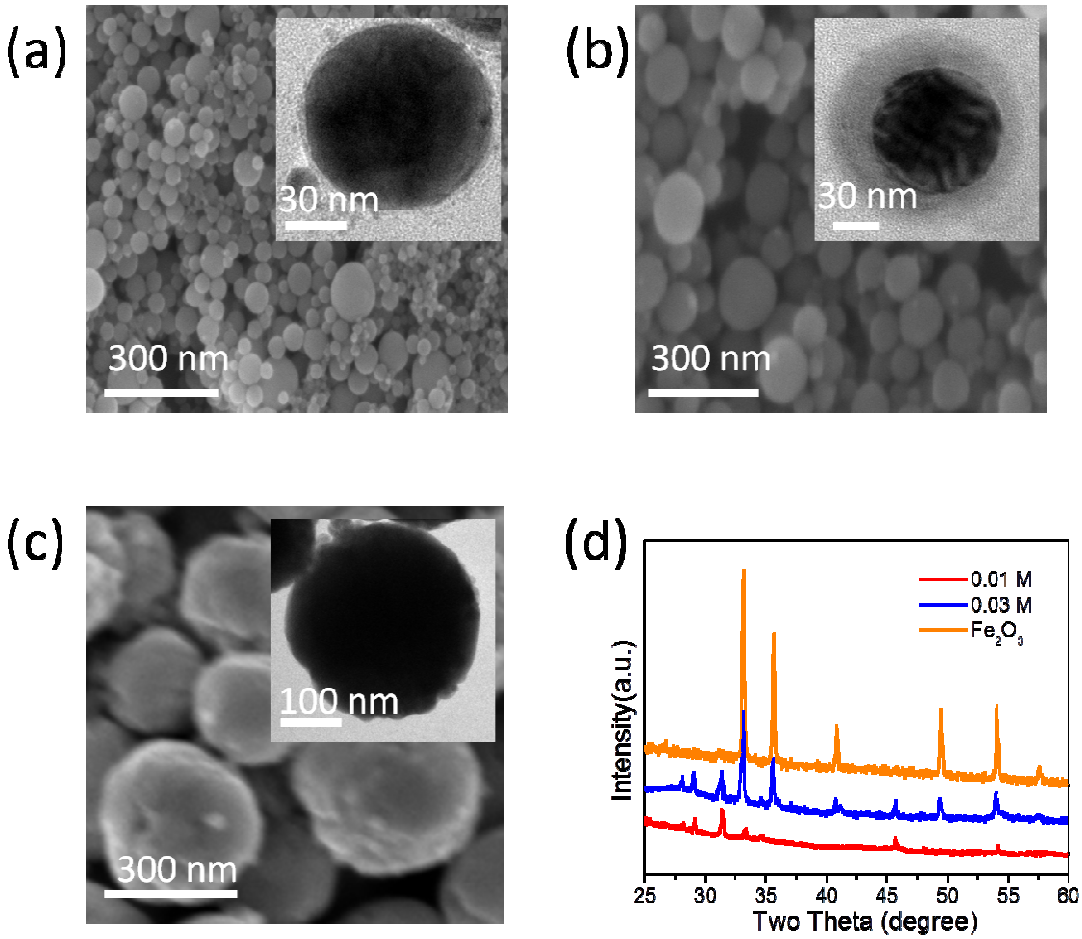

Fig. 7

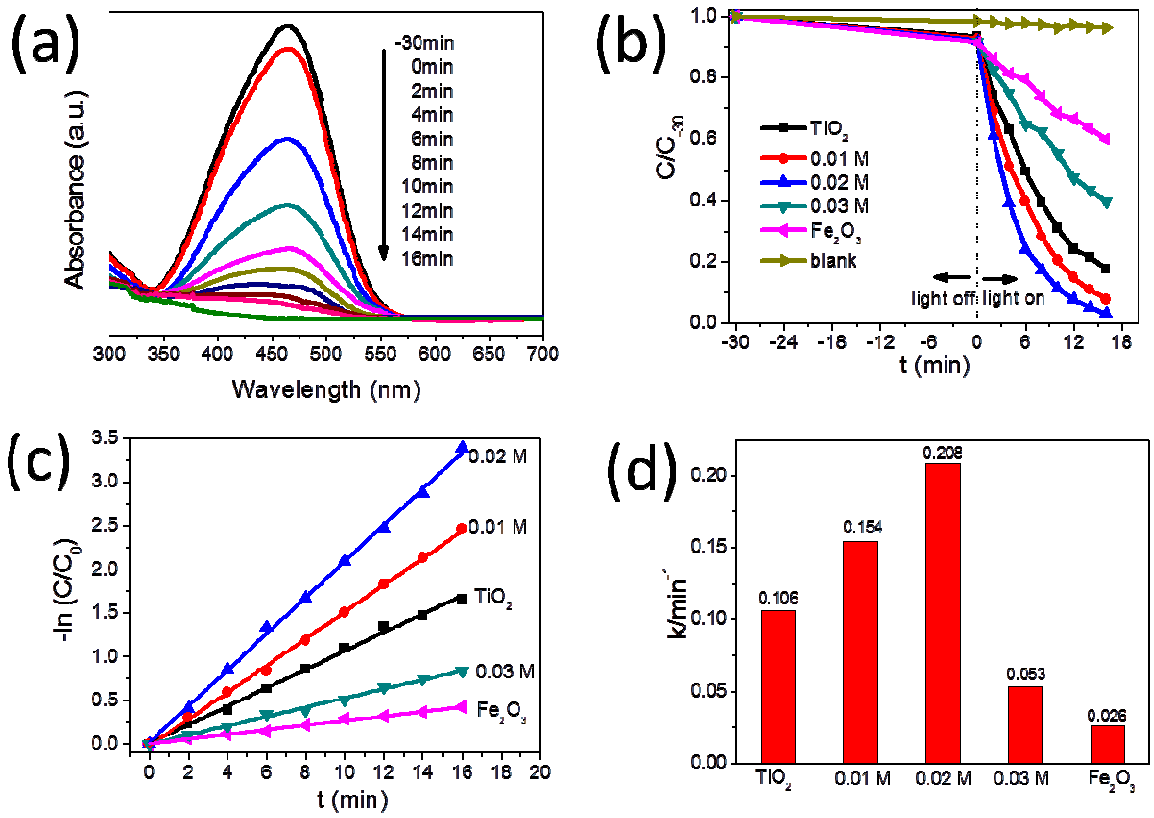

Fig. 8

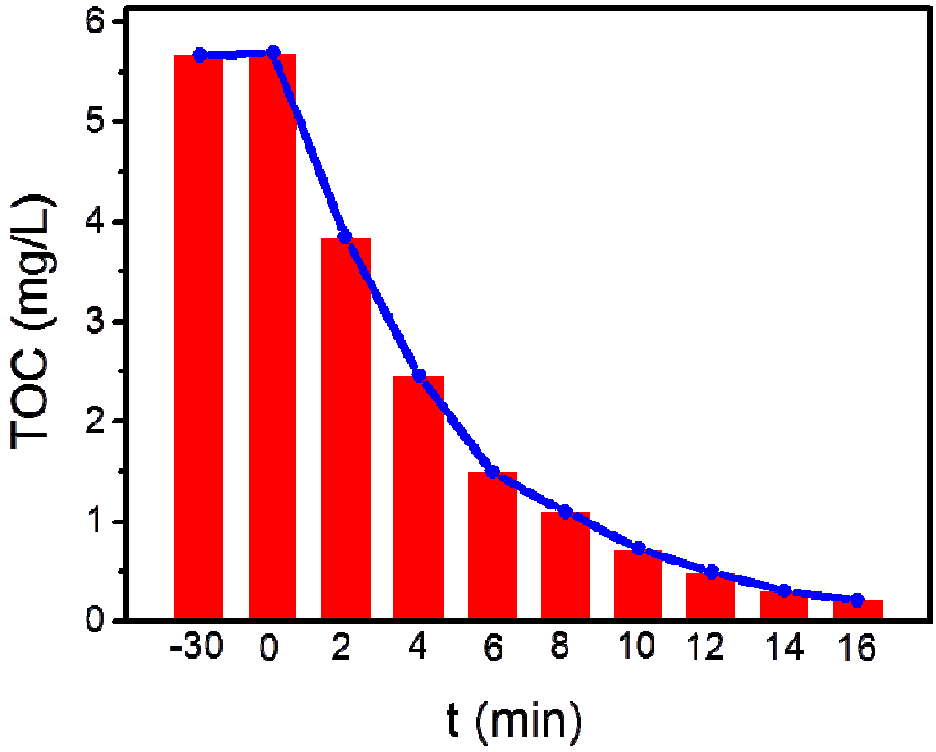

Fig. 9

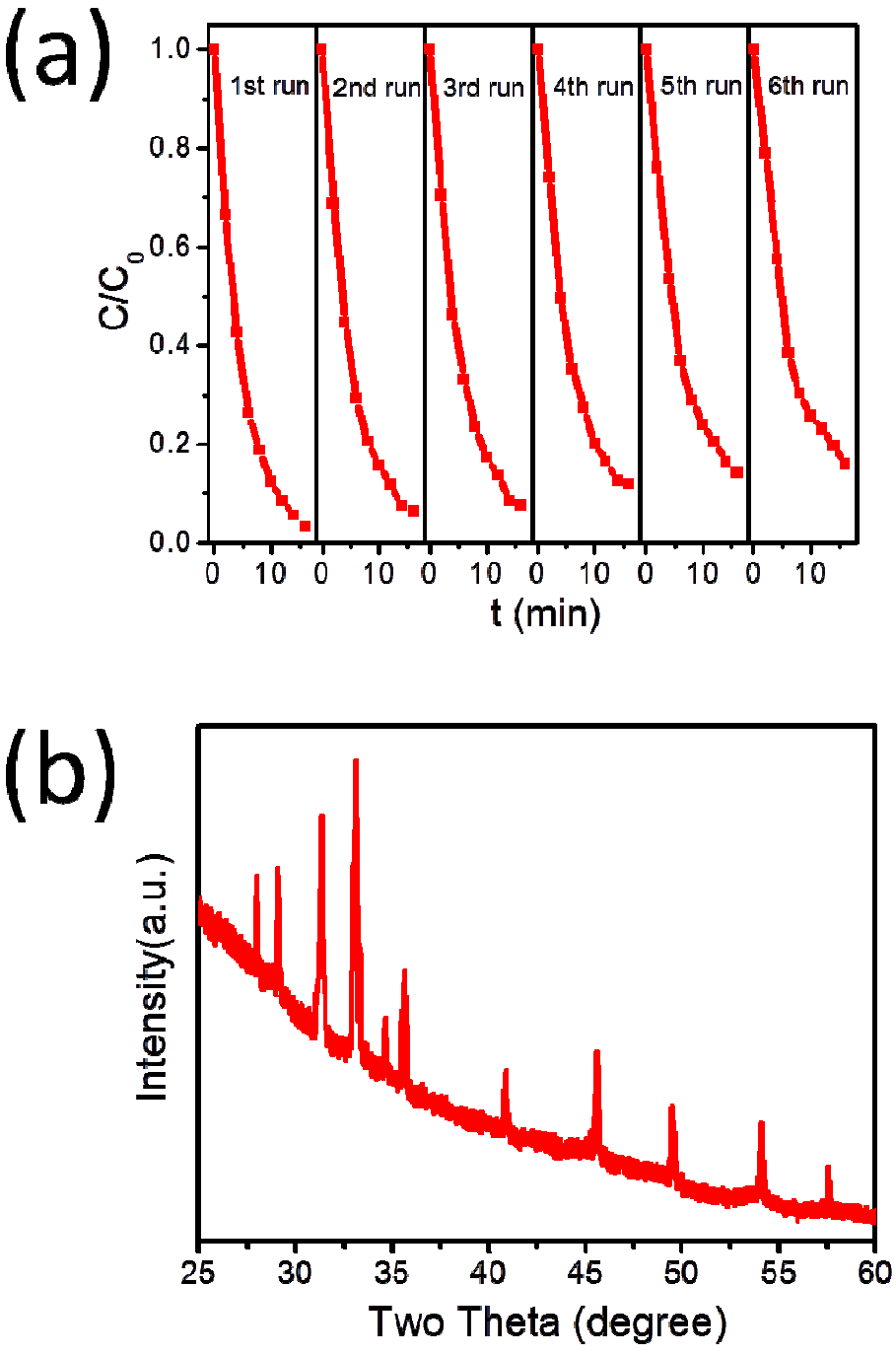

Fig. 10

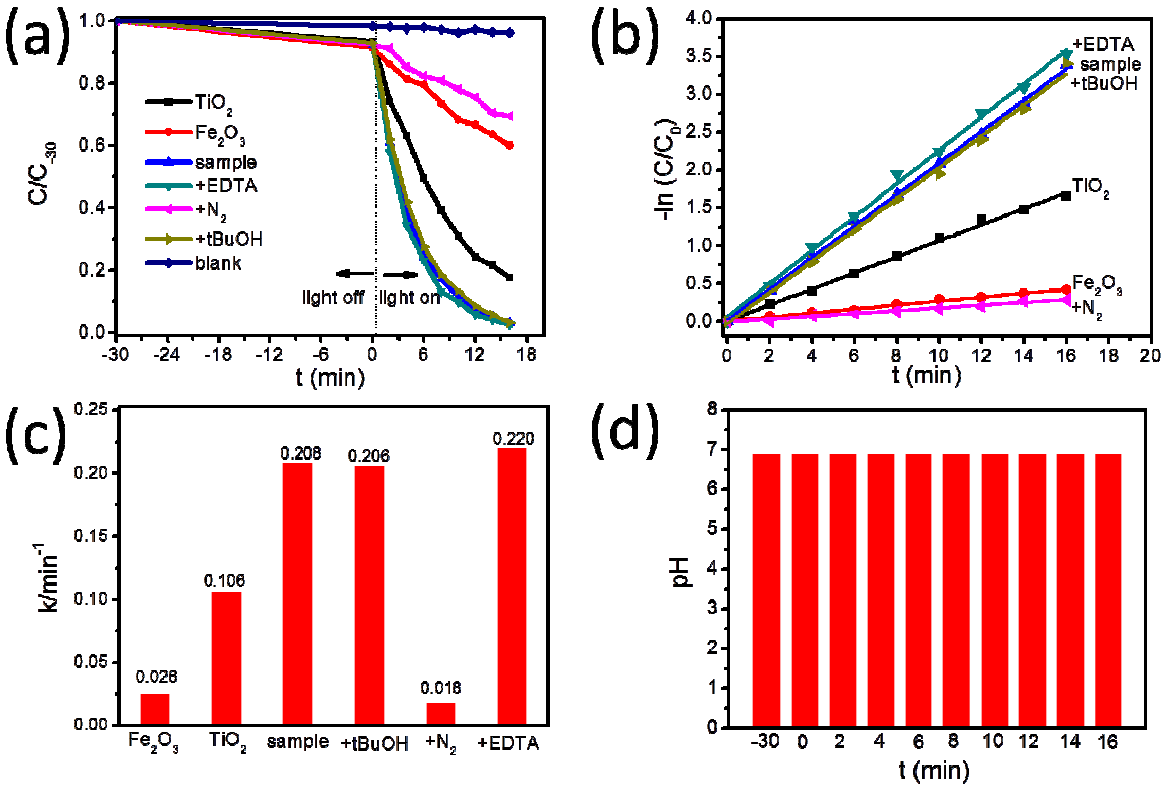

Fig. 11